Fluid Dynamics and Performance of Partially and Fully Shrouded Axial Turbines

L. Porreca
e-mail: luca.porreca@ethz.ch

T. Behr

J. Schlienger

A. I. Kalfas

R. S. Abhari

Turbomachinery Laboratory,
Swiss Federal Institute of Technology,
8092 Zurich, Switzerland

J. Ehrhard
ALSTOM Switzerland Ltd.

E. Janke
Rolls Royce Deutschland

A unique comparative experimental and numerical investigation carried out on two test cases with shroud configurations, differing only in the labyrinth seal path, is presented in this paper. The blade geometry and tip clearance are identical in the two test cases. The geometries under investigation are representative of an axial turbine with a full and partial shroud, respectively. Global performance and flow field data were acquired and analyzed. Computational simulations were carried out to complement the investigation and to facilitate the analysis of the steady and unsteady flow measurements. A detailed comparison between the two test cases is presented in terms of flow field analysis and performance evaluation. The analysis focuses on the flow effects reflected on the overall performance in a multi-stage environment. Strong interaction between the cavity flow and the blade tip region of the rotor blades is observed up to the blade midspan. A marked effect of this interaction can be seen in the downstream second stator where different vortex structures are observed. Moreover, in the partial shroud test case, a strong tip leakage vortex is developed from the first rotor and transported through the downstream blade row. A measurable change in the second stage efficiency was observed between the two test cases. In low aspect ratio blades within a multi-stage environment, small changes in the cavity geometry can have a significant effect on the mainstream flow. The present analysis has shown that an integrated and matched blade-shroud aerodynamic design has to be adopted to reach optimal performances. The additional losses resulting from small variations of the sealing geometry could result in a gain of up to one point in the overall stage efficiency. [DOI: 10.1115/1.2008972]

Introduction

Modern turbomachinery designs aim to increase blade loading and pressure ratio while maintaining the same high efficiency level. This results in a higher power density and lower part count and therefore lower cost. In this perspective, secondary flows and the interactions between leakage and mainstream flow contribute considerably to the overall turbine losses. Particularly, for low aspect ratio blading, it has been shown [1,2] that the flow is highly three dimensional and the secondary effects are often dominant in the overall loss mechanism.

Leakage flows between rotating and stationary parts are commonly reduced with sealing devices such as shrouds and labyrinth seal paths. By lowering the mass flow through the labyrinth seal, a greater proportion of the total flow remains available for work extraction within the blade rows. Labyrinth leakages may account for up to 30% of the total aerodynamic losses in a turbine stage.

Wallis et al. [3] identified four entropy generation mechanisms in the leakage process: fluid entering into the shroud cavity, mixing in the clearance downstream of the fin, mixing with the mainstream flow and non-ideal incidence in the downstream stator row. In their investigation, the aim was to reduce the mixing losses by inserting turning devices into the labyrinth cavity to match the yaw angle of the main stream. However, the experiments showed that the overall efficiency dropped with respect to the reference configuration due to the poor performance of the turning devices.

Peters et al. [4] and Anker and Mayer [5] performed experimental and numerical investigations in a 1 and a half stage low speed axial turbine. They observed a significant incidence variation in

the second stator acted by the leakage flow increasing with the clearance height. Morphis and Bindon [6] reported on an investigation of a one and a half stage axial turbine with unshrouded rotor blades. A reduction of the secondary flows in the second stator was observed due to the tip leakage flow.

Hunter and Manwaring [7] reported a detailed investigation on the effect of the hub leakage in the secondary flow structures of the downstream rotor and stator rows. An upward radial migration of the secondary flow at the hub of the first rotor was detected. Significant changes were observed in the flow field even in this high aspect ratio blading. Some studies focused also on axial compressor leakage influence in the main stream [8,9].

An emerging goal for modern designs is the accurate matching between the cavity flow and the main stream. Integrated blade-cavity-shroud design is instrumental in optimizing aerodynamic performances.

In this work, an analytical study is carried out attempting to isolate the effect of geometrical variations to the flow field and the aerodynamic performance using two test cases, where only the labyrinth seal geometry was changed while the blade geometry and the tip clearance were kept unchanged.

The first test case (PS) is representative of a partial shroud configuration. The second test case (FS) has a classical full shroud arrangement. Global performance is discussed in combination with the associated flow field including an unsteady data analysis for the partial shroud test case (PS). In fact, full shrouds increase the weight at the highest radius leading to increased stresses which rapidly approach the structural limits of the blades and disks. In some cases, mechanical integrity considerations call for a reduction of the shroud weight. Partial shroud designs are therefore used in an attempt to benefit from the advantages of shrouded configurations as well as enjoying reduced weight.
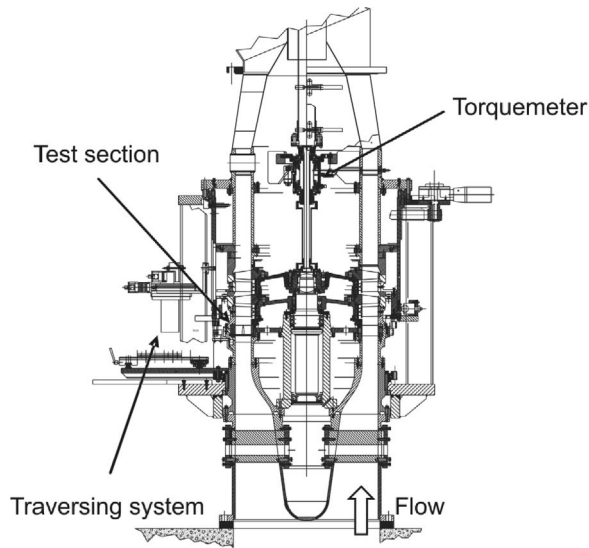
Fig. 1 "LISA" Two stages axial turbine facility

Fig. 2 Schematic of the shroud configuration: (a) partial shroud, (b) full shroud

Experimental Method

Research Facility. The experimental investigation was performed in the research turbine "LISA" at the Turbomachinery Laboratory of the Swiss Federal Institute of Technology Zurich (ETH Zurich). The facility can accommodate a maximum of two stages of an axial turbine. The air loop is of a closed type and includes a radial compressor, a two-stage water to air heat exchanger and a calibrated venturi nozzle for accurate mass flow measurements. A dc generator absorbs the turbine power and controls the rotational speed of the turbine shaft. The first and the second rotor are mechanically decoupled by a twin spool shaft design. The second stage torque is measured by a calibrated torquemeter. In order to achieve the same rotational speed, both shafts are coupled again before the dc generator. A cross section of the turbine is shown in Fig. 1.

The turbine design allows quick and precise assembly and an easy access to the measurement planes. A number of different intrusive and non-intrusive measurement techniques can be applied. The facility is equipped with a four-axis numerically controlled positioning system with ultrahigh precision in every direction. The turbine is normally operated at constant pressure difference across the stages. The turbine entry temperature is controlled to an accuracy of 0.3% and the rpm is kept constant by the dc generator with a range of ±0.02% (±0.5 rpm). In a typical measurement day, the pressure drop is stable within 0.3%. More details regarding the research facility are available in Schlienger [10]. The main operational parameters of the facility are listed in Table 1.

The variation of the labyrinth seal path has been applied to both stages of the two test cases. The partial shroud test case (PS) has two vertical fins and a shroud platform with cutbacks at leading and trailing edges. Conversely, the FS test case adopts an axisym-

metric shroud representative of a modern full-shroud design adapted to the geometrical constraints of the parallel annulus of the facility. The blade geometry as well as the tip clearance of 1% of the blade span is equal for both test cases. A schematic of the shroud configurations is shown in Fig. 2.

Main features of engine-like leakage flows are accounted for, including smooth geometry downstream of the shroud for simulating the reentry and mixing between the leakage and the mainflow streams.

Measurement Technology. Flow parameters including total and static pressure, flow angles velocity components and Mach number are measured at frequencies up to 40 kHz. The steady flow field is measured with miniature five hole probe with a tip diameter as small as 0.9 mm (Treiber et al. [11]). The mainstream flow field is measured using a 1.8 mm tip diameter single sensor fast response aerodynamic probe (FRAP) in virtual multi-sensor mode providing time resolved information (Kupferschmied et al. [12]). FRAP probe technology also provides unsteady temperature measurements at very low frequency (up to 10 Hz). The absolute uncertainties of the used probe techniques are listed in Table 2 (Schlienger et al. [13]).

The FRAP probe used in the investigation misses the third component (pitch) of the flow due to the virtual three-sensor mode. For large pitch angle (±4 deg), an increased error of static, total pressure and Mach number occurs. Temperature measurements obtained with FRAP are affected by an absolute uncertainty of the order of ±0.3 K.

The steady and unsteady turbine flow field has been measured in three planes at the exit of the first rotor, second stator and second rotor, namely A1, A2 and A3 (Fig. 3). The measurement mesh comprises a total of 690 points distributed uniformly in the circumferential direction every 5% pitch (23 points in 1.1 pitches) and 30 points in the radial direction, clustered towards the end walls. Additionally, the second stator steady static pressure distribution was acquired at different blade span as well as the static pressure distribution on both rotor outer casings.

Numerical Method

The simulations were performed using the commercial flow solver FLUENT 6.1, which is based on an unstructured finite volume scheme. Stage coupling is based on the mixing plane tech-

Table 1 Main parameter of "LISA" two-stages axial turbine research facility

Rotor speed [rpm]	2625
Overall pressure ratio	1.38
Mass flow [kg/s]	10.65
Blade count (stator/rotor)	42/42
Aspect ratio	1.8
Outer tip diameter [m]	0.8
Mach number (stator/rotor)	0.35/0.1
Reynolds number (Rotor)	$2*10^5$

Table 2 Uncertainty bandwidth of the used probes

Probe type	ϕ	β	Pt	Ps	Ma
5HP	0.3°	0.3°	60 Pa	130 Pa	0.4%
2D FRAP	0.3°	⋯	100 Pa*	150 Pa*	0.4%*

(* for flow pitch angle $<\pm 4°$)

Fig. 3 Turbine traversing probe planes

Fig. 5 Mass averaged yaw angles at the exit of the first rotor–plane A1–(*a*) absolute, (*b*) relative
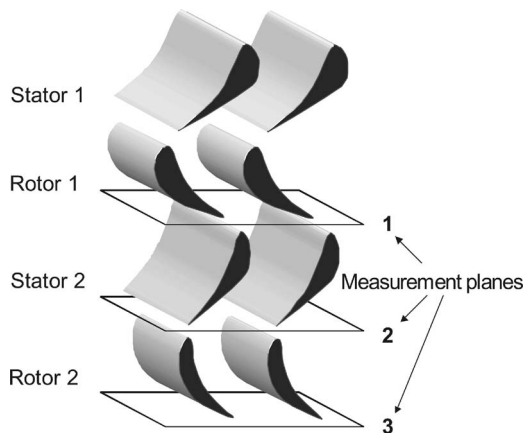
nique, i.e., each fluid zone is solved as a steady-state problem and at prescribed iteration intervals; the flow data at the mixing plane interface are averaged in circumferential direction on both interface boundaries.

The flow was assumed to be fully turbulent and turbulence closure was achieved using the Spalart-Allmaras turbulence model [14], which solves a transport equation for a quantity that is a modified form of the turbulent kinematic viscosity.

To facilitate efficient meshing of the non-axisymmetric partial shroud geometry and to reduce the turn-around time for grid generation, unstructured meshes covering both the main flow path and the tip leakage paths were chosen for both geometries. Following the hybrid meshing strategy of the commercial grid generator CENTAUR, prismatic elements were applied in regions of high solution gradients, and tetrahedra were used elsewhere with pyramids used in some locations to allow for a transition between the prisms and the tetrahedra. The total number of elements for both geometries is about 2.7 million, resulting in an average non-dimensional wall distance $y+$ of 13 and a maximum $y+$ of 49. Figure 4 shows a meridional view of the mesh around to the first rotor shroud for the partial and the full shroud test cases.

Each tip gap was resolved by 25–30 elements in radial direction. Measured total pressure, total temperature and flow angle distributions were prescribed at the inlet to the computational domain. The inlet turbulence intensity of 2% and a turbulent length scale of 0.1 m was chosen to reflect the flow conditions of the test
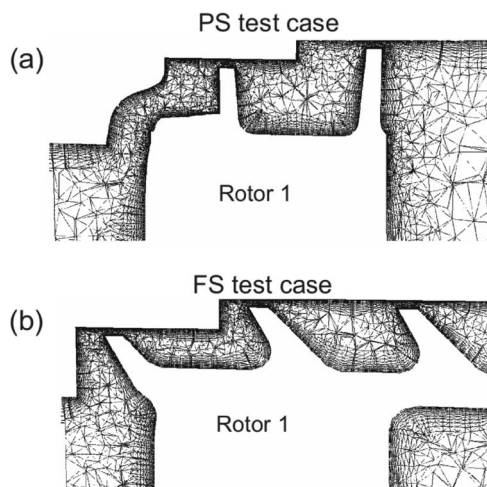
Fig. 4 Spatial discretization in the labyrinth path (*a*) partial shroud, (*b*) full shroud
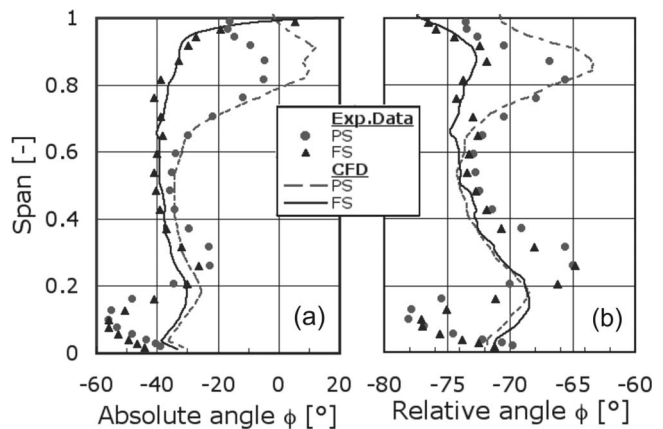
facility. A reference static pressure at hub exit and the radial equilibrium condition were prescribed at the outlet. All walls were assumed to be adiabatic.

Results and Discussion

The experiments were performed keeping the facility at constant pressure drop across the turbine and constant rotational speed. During a preliminary performance analysis, differences in the turbine operational point were observed between the two test cases. A 3% higher mass flow was experienced in the PS. The torque and power measured on the second stage were larger as much as 2%. This result can be explained taking into account reduced end wall coverage of the partial shroud platform in addition to the smaller number of sealing fins. As a consequence, the area available to the fluid is relatively larger at the tip region leading to a variation of the throttling characteristics of the turbine stage. This may have consequences reflected on the work extraction rate and hence to the overall turbine pressure drop at constant mass flow.

The work is presented with the following structure: Steady flow analysis is presented on both test cases comparing measured and predicted data. Additionally, experimental unsteady analysis is performed on the partial shroud (PS) case. Finally a performance comparison and a discussion of the results complete the investigation.

Steady Flow Field Analysis

First Rotor Exit-Plane A1. Leakage flow downstream of the first rotor still retains a large amount of the momentum of the upstream stator as shown in previous investigations (e.g., [3,7]). Therefore, a common design intention is to align this undeflected flow with the main stream in order to reduce the production of entropy in the mixing process. Figure 4 shows the mass averaged absolute and relative yaw angle downstream the first rotor of the two test cases. The flow has the same features until midspan. Closer to the tip in the PS test case, the measured data show that the fluid is underturned from approximately 60% span to the tip.

In this case, a vortex of considerable strength develops due to the trailing edge cut back of the shroud. The principal characteristics of this feature are similar to a tip leakage vortex. This behavior is detected by the overturning-underturning behavior (of the order 10 deg) from the tip to 80% span. In the absence of the shroud platform, the resulting tip gap at the end of the blade channel is of the order of the 10% of the blade span. Hence, the flow is easily moving over the blade tip from the pressure side to the suction side and generating the tip vortex. This feature results in a marked underloading of the rotor blade from approximately 60% to 100% span (Fig. 5).
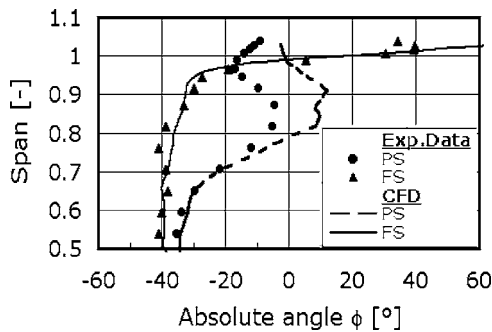
Fig. 6 Absolute mass averaged yaw angles from midspan up to the cavity at the exit of the first rotor–plane A1

Fig. 8 Measured static pressure distribution on the second stator: (a) 75%, (b) 90% span

Remaining swirl is observed at the tip region of the partial shroud test case (PS), therefore the design intention to align the cavity flow with the main stream is only partly achieved in this case. In the full shroud case (FS), the absolute flow angle remains almost constant past 90% span. The flow is appropriately turned and the blading is fully loaded until this point. Closer to the tip region (from 90% to 100% span), the flow is underturned aiming to align to the cavity flow as indicated in Fig. 6.

In both cases a secondary flow structure is detected in the hub region. Previous investigations complementary to the present work [13,15], have shown that the development of the hub passage vortex is greatly affected by the reentry of the labyrinth leakage flow of the upstream stator hub shroud.

Computational fluid dynamics (CFD) calculations show a good agreement with the measured data at midspan. The difference between computed and measured yaw angle in this region is limited in the range of ±0.5° both in the absolute and in the relative frame. At the tip, calculations can correctly predict the yaw angle variation up to the cavity for the FS test case. In the PS geometry, the tip underloading is overestimated by approximately 10°. The underturning-overturning behavior at the hub region is not predicted. This is expected due to the fact that the stator hub leakage flow is not modeled in the CFD calculations. The vortical structures in this location are resulting from the interaction between leakage from the stator cavity and hub rotor passage vortex.

The larger cavity of the PS test case at the exit of the first rotor produces a strong leakage flow interaction with the main stream. Figure 7 shows 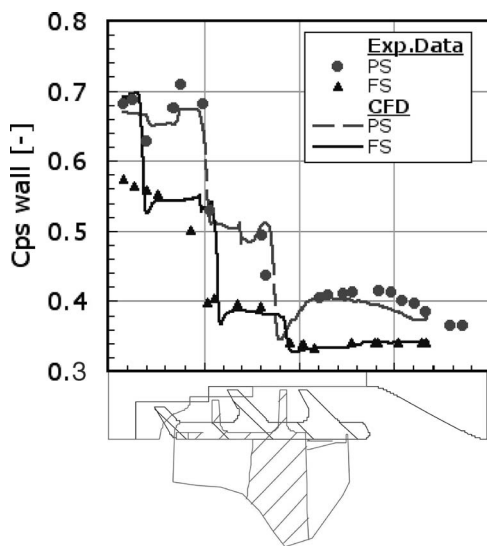the static pressure distribution which has been measured on the outer casing over the rotor. In the PS case, the leakage flow is first expanded in the cavity (slight deceleration in region A) and then accelerated back into the main flow further downstream showing a decreased pressure (region B). The pressure distribution in the end wall outer casing of the second rotor (not shown here) reveals the similar flow features. The leakage flow experiences over both rotor casings the same expansion and re-acceleration together with the mainstream fluid. In the full shroud case (FS), having a smaller cavity, static pressure remains almost constant. Deceleration and acceleration of the leakage jet are not detected other than a low expansion to the downstream static conditions signifying relatively low local mixing. The CFD results confirm this tendency and they agree well with the measurements. The resultant flow is entrained back into the main stream impinging on the downstream leading edge of the stator leading edge. This process affects the incidence angle on the downstream stator leading edge and thereby the loading and the associate stator losses, being reflected on the overall stage performance. These effects are further discussed in the following sections of the present study.

Profile static pressure distribution (Fig. 8) across the stator blades shows a typical negative incidence behavior in the PS test case. This is the effect of the underloading of the PS tip rotor blade region and the incoming of the jet leakage. The incidence variation for the PS case with respect to the design blade angle is of the order of 22 deg and 14 deg at 75% and 90% span, respectively. Therefore, the stagnation point is shifted on the suction side causing a localized pressure increase. This leads to a greater radial pressure gradient from the tip to the hub of the passage with respect to the FS case. The same incidence variation and radial pressure gradient increase was also detected in previous experimental and numerical investigation in a multi-stage environment (Peters et al. [4], Anker and Mayer [5], Gier et al. [16]). However, in those studies this behavior was observed with increased tip clearances while keeping the labyrinth path unchanged.

Mach number and flow angles derived from five-hole-probe (5HP) data combined with static temperature measured by FRAP allow to compute the mass flow. The radial distribution at the exit of the first rotor is presented in Fig. 9(a). Both test cases show very similar profile up to 70% span. Further upstream in the radial direction, the PS case shows increased values between 0.7 and 0.9 span. The leakage mass flow (above 100% span) is, as well, slightly larger. The integrated flow profile shows a difference between the test cases of 4%, consistent with the mass flow measured by the more accurate venturi (3.1%) for the same pressure drop across the turbine.

From the five-hole-probe (5HP) measurements, pitch angle is derived (Fig. 9(b)). In the PS case, the tip leakage penetration into the main flow is clearly shown. From 80% span to the blade tip, negative pitch angles up to −25 deg are measured. In the FS case, pitch angle is almost constant until the blade tip. Negative angle is only detected in the cavity.

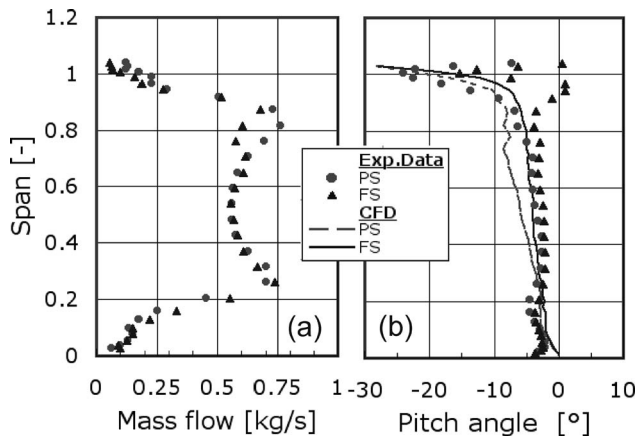Total and relative pressure measurements at the exit of the first

Fig. 7 End wall static pressure coefficient over the first rotor outer casing

Fig. 9 (*a*) **Mass flow distribution,** (*b*) **mass averaged pitch angle at exit of the first rotor–Plane A1**

Fig. 11 Mass averaged (*a*) **total pressure coefficient** (*b*) **yaw angle at the exit of the second stator—Plane A2**

rotor are presented in Fig. 10. Marked differences between PS and FS are detected from 60% span to the tip. In the relative frame of reference, the flow in the PS case shows higher total pressure reduction. This is associated with the strong leakage vortex over the tip at the trailing edge cutback and the larger relative clearance. In the FS case, the reduction of *Cpt* in both absolute and relative frame at 90%–100% span is most likely due to the wake generated by the shroud platform trailing edge rim. CFD calculations predict appropriately the total pressure coefficient in the relative frame and qualitatively in the absolute frame. At midspan, the difference between calculation and measurements are of the order of 2%. However, larger departures are noted at the hub because the hub leakage is not modeled in the computations.

Although at first sight, aerodynamic considerations tend to favor the choice of a full shroud arrangement, the ultimate designers choice is based on the overall performance as well as other competing mechanical integrity issues. In the present analysis, the aerodynamic effects on each individual blade row are assessed, before building the overall performance picture.

Second Stator Exit–Plane A2. The flow detected at the exit of the first rotor is significantly affecting the aerodynamic performance at the exit of the second stator. The flow is similar for both test cases from hub up to midspan. At the hub, the passage vortex is established with typical overturnig-underturning behavior. Further up in the radial direction, a marked underturning-overturning behavior is observed at 70% of the span in the full shroud test case (FS). This feature is caused by the cavity flow from the first rotor
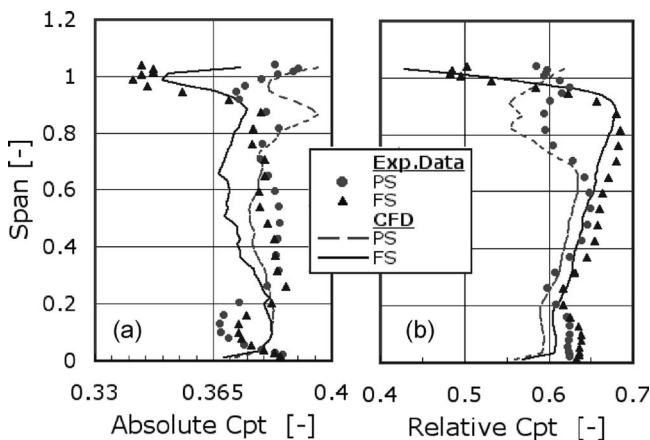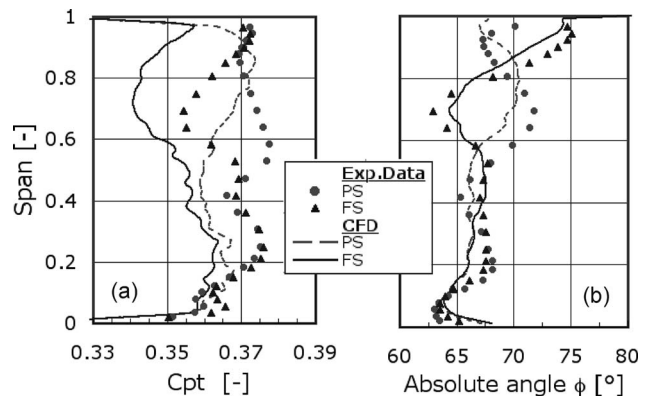
that is accelerated by the reentry channel in the main stream and rolled up with the tip passage vortex (Fig. 11). This vortical structure (named D+E) can be observed in the vector plot in Fig. 12(*b*). In the PS case, the turning acted by the stator row at the tip is reduced as much as 25% with respect to the FS case, having the inlet stator angle a negative incidence. Consequently the overturning-underturning of the tip passage vortex is decreased and observed at 90% span. In the FS case, the variation between underturning and the overturning occurring from 60% up to 100% span is of the order of 25 deg. On the other hand, the same variation in the PS case (observed between 70% and 100% span) is of the order of 10 deg. Moreover, a substantial overall *Cpt* reduction in the PS case appears in the pitch-wise profile in Fig. 11 between mid and 85% span. It can therefore be concluded that the losses associated with this vortex structure are reduced in the PS case.

The strong leakage vortex over the tip at the trailing edge cutback of the rotor tip (PS case) is convected downstream through the second stator. Due to the stronger radial pressure gradient compared to the FS case generated by the negative incidence, the vortex migrates radially towards the hub and detected at midspan at the stator exit, showing the overturning-underturning in Fig. 11(*b*) and the feature named D in Fig. 12(*b*).

The CFD prediction agrees well with the measurements of the yaw angle at midspan (Fig. 11). The prediction is in the range of ±1 deg from 30% to 50% span. Overturning-underturning is also captured at the hub as well as at the tip in both test cases within ±2 deg. The total pressure profile is underestimated except from the hub region. At midspan, the computed *Cpt* is 4% lower compared to the measured data. The higher overall *Cpt* of the PS is predicted but only qualitatively.

Figure 12 shows the steady total pressure coefficient downstream of the second stator together with the secondary flow vectors. Vortex structures are very similar for both test cases up to 40% span. The trailing edge wake is identified in both cases at approximately −20% blade pitch. Structure A is the hub passage vortex that contributes to the total pressure reduction in this region. Structures B and C are related to the blade row and leakage interactions as well as convected secondary flow features and vorticity shedding. In the PS test case, a strong vortex is identified at midspan (C). This structure is thought to be the leakage vortex originating from the first rotor. In the full shroud test case (FS), the moderate leakage vortex is rolled up in the passage vortex and identified in the structure E. The total pressure drop associated with this structure is larger with respect to the PS as previously discussed. This information may be insufficient to draw concrete conclusions about the blading loss generation in this multistage environment. Therefore, unsteady measurements of temperature and pressure derived from the FRAP probe are used. High frequency pressure and low frequency temperature signal are time averaged and combined providing steady entropy information.
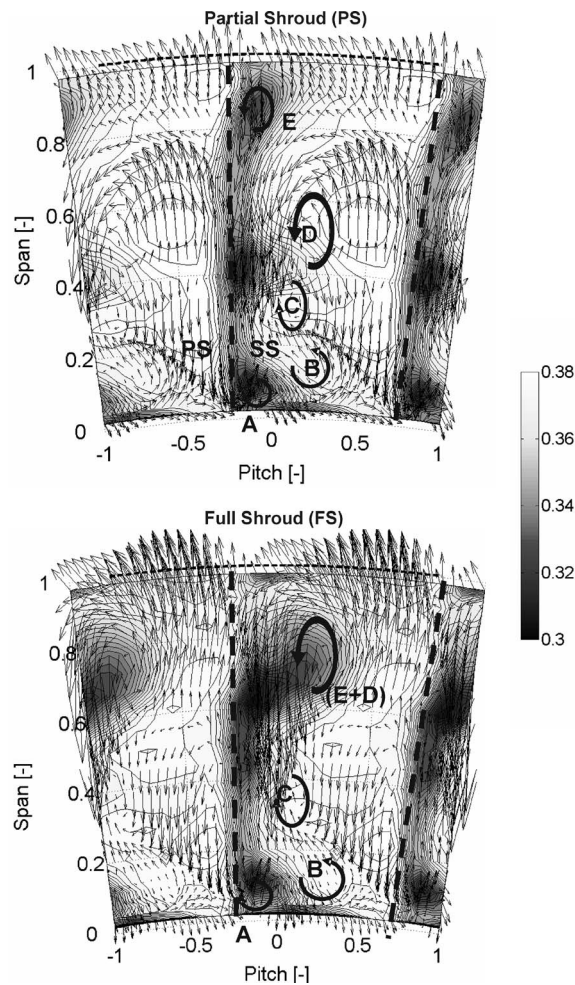

Fig. 10 Mass averaged total pressure coefficient at exit of the first rotor–Plane A1–(*a*) **absolute,** (*b*) **relative**

Fig. 12 Measured total pressure coefficient and secondary flow vector plot downstream of the second stator–Plane A2–(*a*) PS test case, (*b*) FS test case

Fig. 13 Measured entropy function downstream of the second stator—Plane A2—(*a*) PS test case (*b*) FS test case

Entropy evaluation is presented in Fig. 13. The entropy function is defined as $\exp(-\Delta s/R)$, where Δs is derived by the total pressure and total temperature measurements [17].

The reference values are taken in the same plane and selected in order to achieve $e=1$ (no losses), in the minimum entropy value. The various loss cores discussed earlier through the total pressure coefficient plots can be observed in these plots. They can be associated with the vortex structures detected in Fig. 12. As previously discussed, the magnitude of this loss in the passage vortex cores is increased in the FS due to the higher turning. In the PS test case, the strong vortex associate with the trailing edge cut back of the first rotor is creating relatively large losses at a lower radial position. In the partial shroud test case, the entropy function at midspan appears intensified. It is also interesting to notice that the area affected by the high entropy at the tip is quite extended compared to the full shroud case. This behavior cannot be fully appreciated by the total pressure coefficient and may be explained taking into account that the total pressure coefficient does not include any information about the temperature of the fluid.

Close inspection of Figs. 12 and 13 reveals that three of the vortical structures (A, C and E) are associated with intense and localized increased loss generation. The loss levels associated with the other two features (B and D) are relatively lower and diffused raising the background level of entropy.

At lower half of the span including the hub, both test cases show the same picture in terms of both loss and vortically moving fluid. However, in the top part of the plot, it can be noticed that
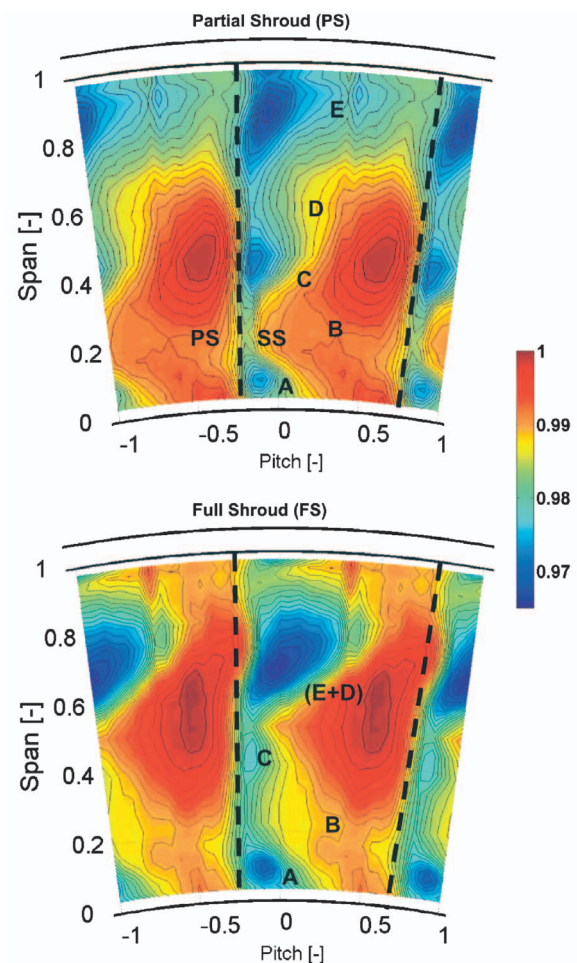
there is a radial migration of lossy fluid induced by the strong interactions between the vortices and the radial pressure gradient variation. This affects the way that vorticity is shed from the trailing edge in the two cases. The intensity of loss generation in the midspan is therefore affected by the process of tip vortex formation.

In the FS test case, the tip vortex is strong and dominant covering the area between 60% and 80% span. In the PS test case, a combination of effects, as described earlier, pushes the initially generated vortex inward with two consequences. First, the midspan region is dominated by a double formation of counter rotating vortices that invokes compressing forces on the wake fluid, resulting in increased localized loss production. Second, the radial migration of the initial tip vortex gives space for the development of the loss core due to the indigenous passage vortex of the second stator (E in Fig. 12(*a*)). The latter vortical structure has strong similarities to a tip leakage vortex with the associate consequence to additional loss generation.

Unsteady Flow Field Analysis of the PS Test Case.

Unsteady Analysis—First Rotor Exit—Plane A1. Figure 14 shows the measured pitchwise mass-averaged variation of the yaw angle as a function of the blade span and the blade passing period. The maxima and the minima of the flow angle together with the relative angle change are also displayed.

The steady measurements derived from the 5HP data are presented superimposed to the angle variation, In the entire span, the steady value is in between the minima and the maxima of the
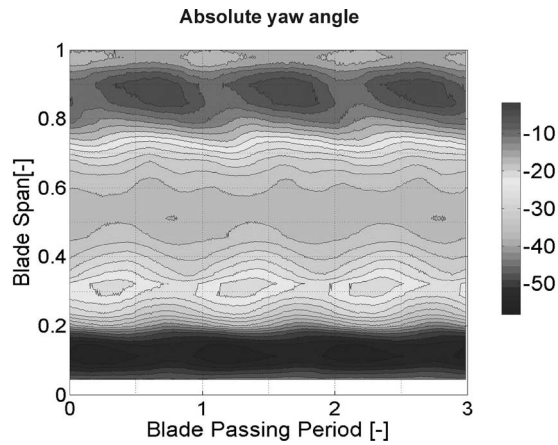
Fig. 14 Experimental time-distance diagram of the mass-averaged absolute yaw angle at the exit of the first rotor in three blade passing period (PS test case)—Plane A1

unsteady measurements, highlighting the accuracy and consistency of the data set derived from the two independent measurement techniques. The overturning-underturning is clearly observed from 10% to 30% span. At the tip region, yaw angles up to -10 deg underline the rotor underloading. The variation of the angle has the same period of the blade passing. This is the result of the variable position of the rotor relative to the downstream stator row. This blade phase results in a sinusoidal variation of the throttling rate of the turbine. From Fig. 14 can be observed that the angle variation is of the order of 8 deg from 20% to 35% span. This is the mark of the passage vortex detected at hub. The large yaw angle variation at 90% span (up to 7 deg) in Fig. 15 and the relative Cpt reduction at the same span (Fig. 16) is consistent with the behavior of the tip leakage vortex. At midspan, where secondary flows are less evident, the angle variation is significantly reduced being of the order of 2 deg.

The development of a double vortex structure is observed at the hub in Fig. 16. As shown in parallel clocking investigation (Behr et al. [18]) this behavior might be related to structures originated in the first stator row and transported through the rotor blade channel. The study also reveals that these features are dependent from the first stator index position with respect to the second stator. The wake seen at $T/T_0=0$ in Fig. 16 is significantly reduced due to the effect of the relative position of the downstream stator. From time $T/T_0=0.5$ to $T/T_0=0.833$, the total pressure reduction due to the wake is overtaken by the pressure rise due to
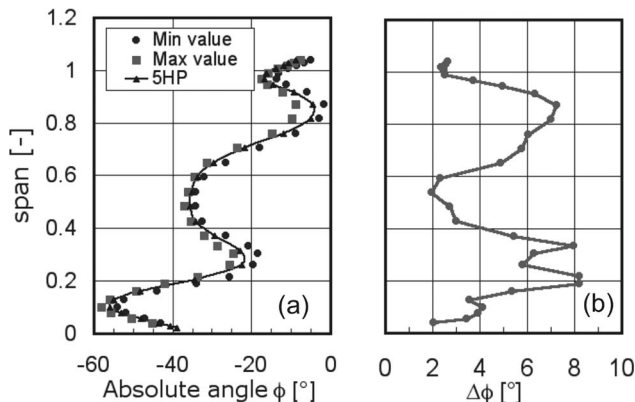

Fig. 15 Experimental mass-averaged yaw angle variation in three blade passing period at the exit of the first rotor. (PS test case)–Plane A1—(a) minimum and maximum values and 5HP measurements (b) variation range.
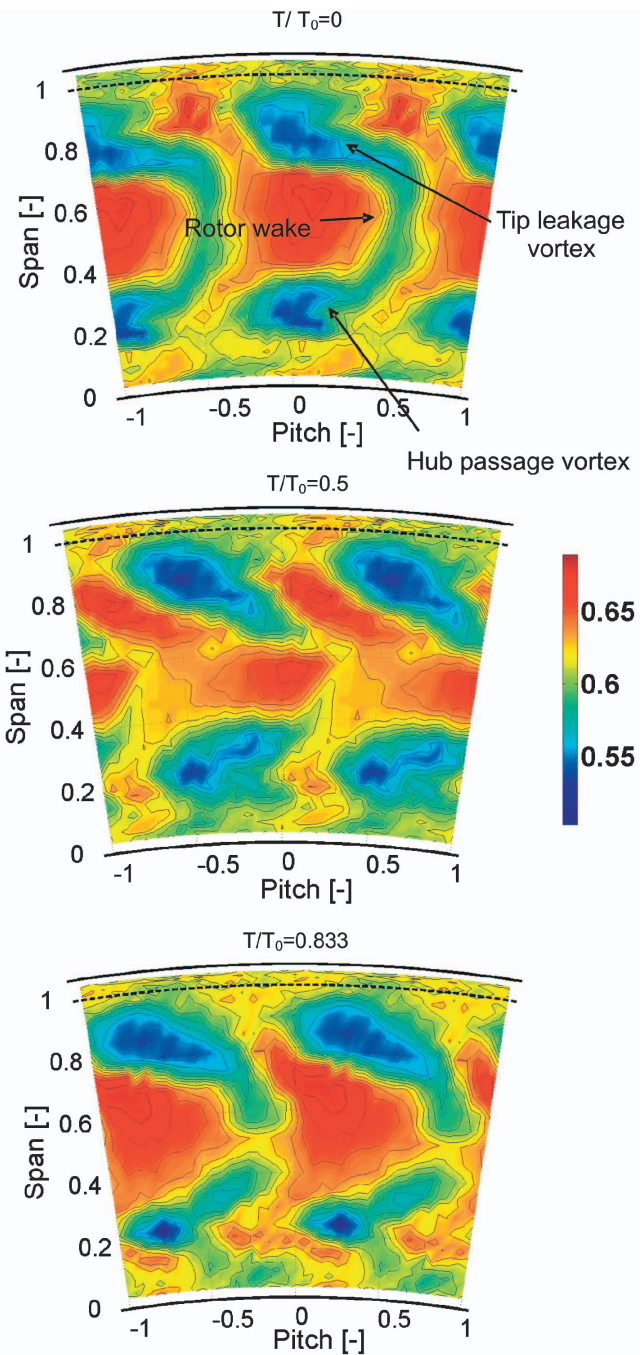

Fig. 16 Experimental time dependent relative total pressure coefficient in one blade passing period at the exit of the first rotor (PS test case)—Plane A1

the stator leading edge. However, the vortex of the leakage flow is continuously produced and is not influenced by the potential field. The large core at 70% span corresponding to the tip leakage vortex is present during all the blade passing period. This indicates that the secondary flows are resistant to the potential pressure field and the associated losses are higher than the losses associated with the blade wake.

Unsteady Analysis—Second Stator Exit—Plane A2. The unsteady measurements show the time dependent behavior of the flow structures identified by the steady analysis. Due to the presence of the first turbine stage, the inlet to the second stage is characterized by a highly three-dimensional pattern that affects the flow field
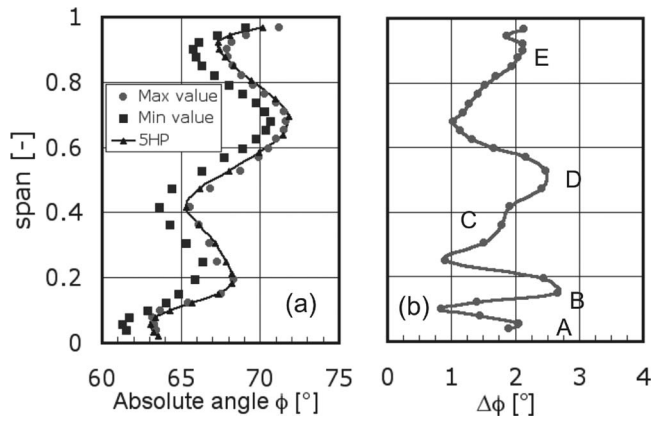
Fig. 17 Experimental mass averaged yaw angle variation in three blade passing period at the exit of the second stator (PS test case)—Plane A2—(a) minimum and maximum values and 5HP measurements, (b) variation range
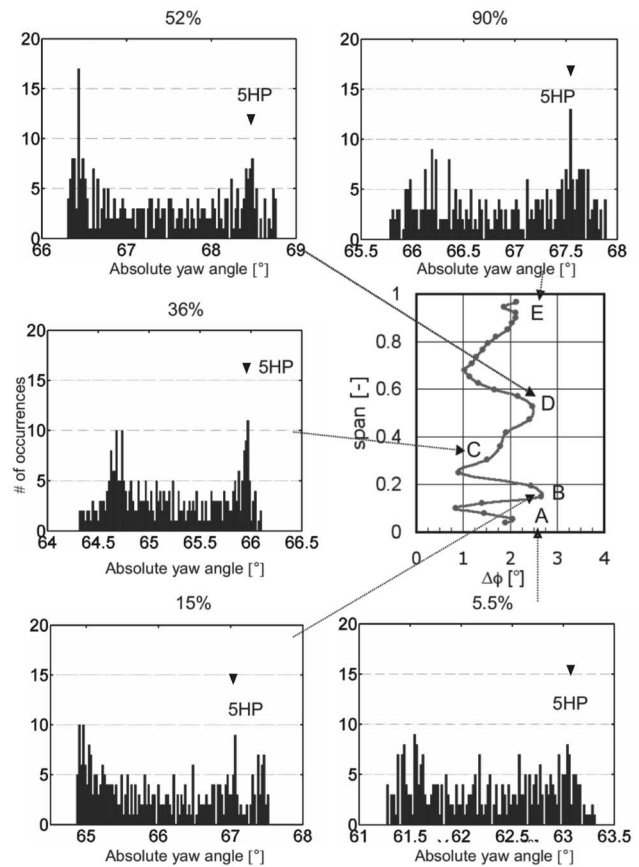

Fig. 18 Frequency of occurrence of the measured unsteady absolute yaw angle at 5.5%, 15%, 36%, 52% and 90% span at the exit of the second stator (PS test case)—Plane A2. Symbols show the 5HP measurements.

downstream this blade row. Secondary flow structures are predominant and they interact significantly with the main flow. Figure 16 shows the maximum and the minimum values of the yaw angle downstream the second stator. Steady data (from 5HP measurements) and relative variation are presented, in the same fashion as for the first rotor exit. In the entire span, the steady values are in between the variation.

The secondary flow structures observed in Fig. 12 from the steady measurements are also identified in the pitchwise average plots. In addition, the range of unsteady variation can be appreciated. The envelop of angle variation is shown in Fig. 17 between the maximum and the minimum angles. The flow angle variation is plotted as a difference $\Delta\phi$ showing that the maximum variation is limited to 2.7 deg. However, at the stator exit, this variation involves a significant momentum difference, owing to the high swirl. The flow features marked (A to E) in Fig. 17 correspond to the equivalent lettered regions of Fig. 12.

A marked result that can be appreciated from Fig. 17 is that the pneumatically averaged data (5HP) follow closely the trend of the unsteady data. Moreover, the agreement is very close to the maximum value of flow deflection.

The outcome of the foregoing discussion led to the statistical analysis of the unsteady variation of the flow angle in order to establish the relation between the pneumatically averaged data and the variations detected by the unsteady technique. The frequency of occurrence distribution of the unsteady flow angle results was constructed at each and every blade span position. The results are shown in Fig. 18. Five span locations are selected corresponding to the yaw angle variations maxima as described earlier in this section. In the mathematical sense, the distribution of the five-hole probe (5HP) data should asymptotically tend to a Dirac delta function. The pneumatically averaged data were therefore marked on the plot with a single point symbol. The physical characteristics of the measured distributions are discussed in view of their consequences to the designer's choices. The first interesting observation is that the distributions are bi-modal. In simple terms, this means that they show two peaks that have high probability of occurrence. The immediate consequence of the bi-modal distributions is that the most frequent values do not correspond to the average value. From the designer's perspective, this means that for most of the time the flow direction deviates from the mean. In the test case under consideration, this is of the order of 2 deg and 8 deg at the stator and rotor exit, respectively. At the rotor exit, the flow angle variations are higher but the tangential momentum difference is of the same order owing to the lower absolute swirl, compared to the stator exit.

As seen in Fig. 17, the 5HP measurements indicate the angle with the highest flow deflection. Cross comparison with Fig. 18 reveals that this coincides with the highest of the two most frequent angle values in the selected regions. It is therefore concluded that the 5HP measurements in regions of high vorticity tend to underestimate the deviation angle. Moreover, the leading edge design of the downstream rows should take into account a periodical incidence variation (with a frequency of 1.8 kHz) of 2 deg–3 deg at the stator exit and up to 8 deg at the rotor exit. This angle variation affects the local span loading as discussed in the performance analysis.

Performance Analysis

Efficiency. Mechanical method is used to evaluate second stage efficiency. Second rotor torque is measured by a torquemeter at five samples/s during the entire time of the data acquisition while the mass flow is continuously acquired during the measurements. The pressure ratio P_{03}/P_{01} is calculated by mass averaging the inlet total pressure in the area at exit of first and the second rotor. By referring the measured shaft power to the isentropic power provided by the fluid, the efficiency can be evaluated. In the current arrangement, mechanical dissipation and heat transfer terms are negligible. The torquemeter is in fact directly connected with the second stage shaft (power dissipation in the bearing is negligible) and the turbine reaches a constant thermal state over the running time. The following equation is used to calculate the aerodynamic efficiency:

$$\eta_{second\_stage} = \frac{M\omega/\dot{m}}{\bar{\bar{T}}_{01}C_p\left(1 - \frac{\overline{\overline{P_{03}}}^{\gamma-1/\gamma}}{\overline{\overline{P_{01}}}}\right)}.$$

The facility is open to the atmospheric pressure at the turbine exit. The turbine pressure drop oscillates with a variation of ±0.3% during a typical 10 h of operation. The measured pressures are corrected with a standard day condition.

The error analysis (Pfau, [19]) shows that the absolute overall uncertainty range on the efficiency (for a given geometry) is equal to 0.6%, while the relative uncertainty range between two test cases is equal to 0.3%.

The loss coefficient within the second stator passage is estimated for both test cases by the following equation:

$$ Y = \frac{(\overline{\overline{P_{01}}} - \overline{\overline{P_{02}}})}{(\overline{\overline{P_{02}}} - \overline{\overline{p_2}})}, $$

where $\overline{\overline{P_{01}}}$ and $\overline{\overline{P_{02}}}$ represent the mass averaged second stator inlet and outlet total pressure, $\overline{p_2}$ is the stator static outlet pressure.

It was observed that the losses in the second stator are increased by almost 1% in the full shroud test case when compared to the partial shroud geometry. In the latter case, two opposing effects are occurring. On one hand, a strong negative incidence is detected from 60% to 100% span in the stator blade. This incidence mismatch is obviously increasing the profile losses at those locations. On the other hand, the flow turning in this region is decreased by around 25% when compared to the full shroud case. Therefore, the losses associated with the tip passage vortex are reduced. The extent of these two effects shows that the secondary flow losses reduction is larger than the increase of the profile losses. This result again illustrates that for a low aspect ratio high turning blade row, the vortical structure effects are predominant compared to other loss generation mechanisms.

Despite the second stator losses increased in the FS case, the second stage efficiency improves compared to the partial shroud case of 1%. This improvement can be attributed mainly to the increased loading of the tip of the rotor blades. The strong tip leakage vortex is not occurring anymore in the full shroud geometry due to the covering of the blade channel. Additionally, flow at the blade tip shows an improved matching with the leakage jet reducing mixing loss generation.

In order to have a qualitative picture of the aerodynamic performances and to relate them to the flow field, the spanwise efficiency variation is calculated with classical thermodynamic method

$$ \eta(r) = \left(1 - \frac{\overline{T_{03}}}{T_{01}} \right) \Big/ \left(1 - \frac{\overline{P_{03}}}{P_{01}} \right)^{\gamma-1/\gamma}. $$

The relative uncertainty in the efficiency is directly related to the temperature drop relative uncertainty. With a total temperature drop of the order of 10°C, the relative uncertainty in the efficiency is higher than in the mechanical method and of the order of ±1%. However, this procedure allows detecting the performance increase/decrease at different span locations. Figure 18 shows the efficiency change between the partial shroud test case (as a reference value) and the full shroud case. The calculations are derived by interpolating the measured and spanwise averaged pressure, temperature and mass flow distribution. Radial efficiency distribution is then evaluated along streamtubes between the second stage inlet and outlet and then compared.

The variation is minimal up to midspan, underlining that the flow field and the aerodynamic performances are unchanged. The effect of the different shroud configuration is detected starting from 60% span. Closer to the tip, the full shroud case (FS) shows a significant improvement.

The difference between the mass averaged efficiency values is of the order of 2%, consistent with the value derived by the more accurate mechanical method.

Power. The local loading coefficient is derived from the unsteady data as follows. First, the time dependent yaw angle is derived from the unsteady measurements downstream of the first
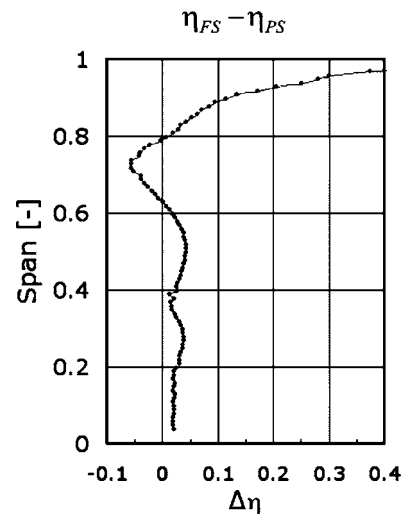

Fig. 19 Measured spanwise efficiency change between FS and PS test case

and the second rotor. Second, the minimum and the maximum values of this angle are derived from the pitchwise mass averaged data at each span position $(\overline{\phi}_{\max}, \overline{\phi}_{\min})$. Then velocity is derived from the local Mach number and the static temperature $(V_{\max}, V_{\min})$. The loading coefficient is then obtained as follows:

$$ \overline{\psi}_{\max,\min} = \frac{\Delta \overline{V}_{\phi\max,\min}}{u} $$

Figure 19 shows the loading variation. In Fig. 20(a), the local minimum and the maximum loading coefficient is normalized by the mean value at midspan. The variation is almost negligible close to midspan where the flow is relatively not affected by the secondary structures. However, a variation up to 15% with respect to the averaged value is detected in the hub region. This unsteady aerodynamic loading enhances vibrations and blade stresses at each blade-passing period (1.8 kHz).

From the time dependent signal, the isentropic enthalpy drop has been also calculated as a function of the blade passing period (Fig. 21). This variation of work extraction implies that the blades experience a sinusoidal force along the span with a variation up to
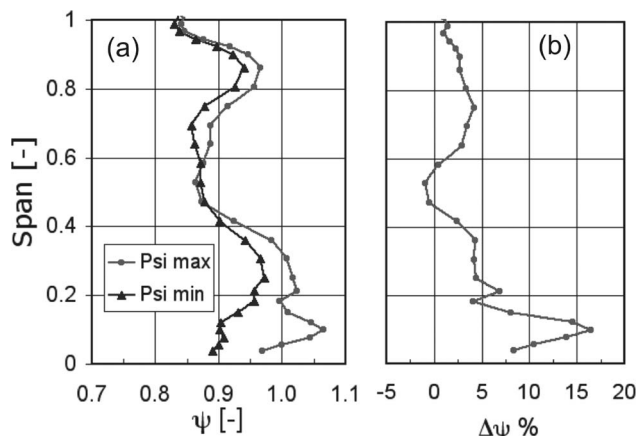

Fig. 20 Measured loading coefficient variation across the second rotor in three blade passing periods—PS test case—(a) minimum and maximum values, (b) variation range
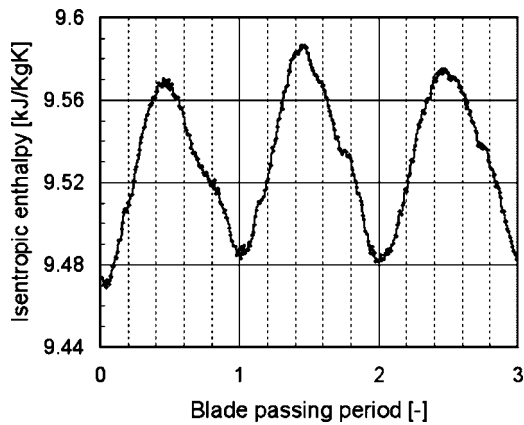
Fig. 21 Measured isentropic enthalpy drop across the second stage—PS test case

0.5%.

The mechanical design of the blade could take advantage of this analysis in order to evaluate correctly the vibration modes and improve the rotordynamics of the bladed disks.

Summary and Discussion

Typical pressure ratio and temperature ranges of this experimental facility are far from the actual engine conditions. However, the experiments and the simulations indicate that the shroud and labyrinth path may have a significant impact on the overall performance and, consequently, these issues need particular attention during the design process. Design tools and methodology can then be validated. The subsequent transfer from the test bench (where the present accurate and reliable measurements were performed) to engine conditions is commonly done by means of CFD.

In a multi-stage environment, the flow field within and after low aspect ratio blading is highly three-dimensional and unsteady. The classical understanding of the secondary flow behind a cascade based on uniform inlet flow may not be fully representative of such flow regimes. The second stage is subjected to unsteady inlet boundary conditions imposed by the nonuniformity of the first stage flow structures. Vortex-wake interactions, potential field of downstream rows and leakage flows have a primary effect on the performance of the downstream rows.

From the present analysis it follows that an optimal aerodynamic design has to involve different parameters that take into account the nonuniformity of the second stage inlet. Several aspects have to be considered, including shroud design, blade loading, second stator leading edge geometry, efficiency.

Despite the fact that the blade geometry and the tip clearance remained unchanged, in the PS case, large deviation between the blade angle and the measured flow in the tip region has been detected. Although aerodynamically superior, the use of full shrouds is not always feasible due to mechanical constrains. In such situations, partial shrouds may be employed. In all these cases, and particularly for the partial shrouds, an integrated blade-shroud design should be adopted. In the PS case, a different blade profile could be designed at the tip in order to increase the loading on the front part. With this approach, the localized tip leakage at the trailing edge cut back may be reduced driven by a reduced pressure difference across the tip, while loading at other span-1 would be increased.

Conclusions

A comprehensive investigation on two test cases with identical turbine blade geometries with a partial and a full shroud arrangement has been conducted. A unique comparative study was performed in order to address the effect of the leakage flow in the flow field and in the overall performance. Owing to the application of consistent experimental techniques supported by numerical methods, fluid dynamics and performance of partially and fully shrouded turbines have been studied.

Unsteady measurements show that in the partial shroud test case a tip leakage vortex is continuously produced in the first rotor tip region while the rotor wake intensity is modulated (and even cancelled) by the potential effect of the downstream stator. Statistical analysis showed that in the yaw angle distribution the mean value is not always the most frequent in the vortex region. The angle distribution is bi-modal with two individual peaks in the range of ±1.5 deg at the second stator exit and ±4 deg at the first rotor exit. The 5HP measurements fall closer to the high probability peak corresponding to the maximum flow deflection. Unsteady aerodynamic loading is derived for the second rotor showing a variation of the work coefficient up to 15% at the hub.

The CFD simulation shows a good agreement with the measured data at midspan in all aerodynamic parameters for the first stage. The discrepancy with the experimental data is of the order ±1 deg in the yaw angle and ±1% in total pressure. At the hub endwall, vortex structures are not captured because the hub leakage flow is not taken into account in the calculation.

Accurate performance measurements show an improvement of the overall second stage efficiency for the full shroud test case (FS) of the order of 1%. The improved control on the blade loading on the rotor and the matching of the cavity flow with the main stream is at the root of this result. However, the second stator experiences a lowered performance compared with the partial shroud test case (PS) of about 1%. The reason for this behavior is the increase of the tip passage vortex loss due to the increase of the turning in the region between 60% and 100% span. Despite the decrease of the profile losses due to the reduction of the negative incidence at the tip, the overall second stator losses are increased with respect to the partial shroud test case. Hence, tip leakage flow can have a significant effect on the secondary flow development in the subsequent blade rows. Leakage jets can thus be used in order to tune the secondary flows and eventually reduce their intensity.

The present study suggests that turbine designers need to perform an integrated time-dependent analysis of the shroud-tip area in order to maximize performance. Particular attention needs to be paid to the matching between the shroud and the blade geometry design. Reentry and mixing of the jet leakage into the main stream can have a critical impact on the flow field and, consequently, on the stage performance. As shown in this work, an improvement up to 1% in the overall stage efficiency can be achieved.

Nomenclature

Cp = specific heat at constant pressure
Cpt = total pressure coefficient
$(P_{0meas}-P_{SExit})/(P_{0Inlet}-P_{SExit})$
Cps = static pressure coefficient
$(P_{Smeas}-P_{SExit})/(P_{0Inlet}-P_{SExit})$
$\dot{m}$ = mass flow

M = second stage torque
P = pressure
R = perfect gas constant
Δs = entropy
T = temperature
T/T_0 = blade passing period fraction
V = flow velocity
PS = partial shroud test case
FS = full shroud test case
5HP = five-hole probe
FRAP = fast response aerodynamic probe

Greek

β = pitch angle
γ = isentropic exponent
η = turbine second stage efficiency
ϕ = yaw angle
ψ = loading coefficient
ω = rotational speed

Subscripts/Superscripts

0 = total conditions
S = static conditions
$1,2,3$ = measurement plane $A1$, $A2$ and $A3$
$\bar{\bar{P}}, \bar{\bar{T}}$ = mass and area averaged data
$\bar{P}, \bar{T}$ = mass pitchwise averaged data
min,max = minimum and maximum value
ref = reference value

References

[1] Langston, L. S., 2001, "Secondary Flows in Axial Turbines—A Review," *Heat Transfer in Gas Turbine Systems*, pp. 11–26.
[2] Chaluvadi, V. S. P., Kalfas, A. I., Banieghbal, M. R., Hodson, H. P., and Denton, J. D., 2001, "Blade Row Interaction in a High Pressure Turbine," AIAA J., **174**, pp. 892–901.
[3] Wallis, A. M., Denton, J. D., and Demargne, A. A. J., 2001, "The Control of Shroud Leakage Flows to Reduce Aerodynamic Losses in a Low Aspect Ratio, Shrouded Axial Flow Turbine," ASME J. Turbomach., **119**, pp. 1–8.
[4] Peters, P., Breisig, V., Giboni, A., Lerner, C., and Pfost, H., 2000, "The Influence of the Clearance of Shrouded Rotor Blades on the Development of the Flow Field and Losses in the Subsequent Stator," ASME Paper No. 2000-GT-478.
[5] Anker, J. E., and Mayer, J. F., 2002, "Simulation of the Interaction of Labyrinth Seal Leakage Flow and Main Flow in an Axial Turbine," ASME Paper No. GT-30348.
[6] Morphis, G., and Bindon, J. P., 1995, "The Flow in a Second Stage Nozzle of a Low Speed Axial Turbine and its Effect on Tip Clearance Loss Development," ASME J. Turbomach., **117**, pp. 571–577.
[7] Hunter, S., and Manwaring, S., 2000, "Endwall Cavity Flow Effects on Gaspath Aerodynamics in an Axial Flow Turbine: Part I—Experimental and Numerical Investigation," ASME Paper No. 2000-GT-651.
[8] Wellborn, S. R., 2001, "Details of Axial-Compressor Shrouded Stator Cavity Flows," ASME Paper No. 2001-GT-495.
[9] Demarge, A. A. J., and Longley, J. P., 2000, "The Aerodynamic Interaction of Stator Shroud Leakage and Mainstream Flows in Compressors," ASME Paper No. 2000-GT-570.
[10] Schlienger, J., 2003, "Evolution of Unsteady Secondary Flows in a Multistage Shrouded Axial Turbine," Ph.D. thesis No. 15230, ETH, Zurich, Switzerland.
[11] Treiber, M., Kupferschmied, P., and Gyarmathy, G., 1998, "Analysis of the Error Propagation Arising From the Measurements With a Miniature Pneumatic 5-Hole Probe," XIVth Symposium on Measuring Techniques for Transonic and Supersonic Flows in Cascades and Turbomachines.
[12] Kupferschmied, P., Köppel, O., Gizzi, W. P., and Gyarmathy, G., "Time Resolved Flow Measurements With Fast Aerodynamic Probes in Turbomachinery," Meas. Sci. Technol., **11**, pp. 1036,1054.
[13] Schlienger, J., Pfau, A., Kalfas, A. I., and Abhari, R. S., 2003, "Effect of Labyrinth Seal Variation on Multistage Axial Turbine Flow." ASME Paper No. GT-2003-38270.
[14] Spalart, P., and Allmaras, S., 1992, "A One-Equation Turbulence Model for Aerodynamic Flows," Technical Report No. AIAA-92-0439, American Institute of Aeronautics and Astronautics.
[15] Schlienger, J., Kalfas, A. I., and R. S. Abhari, 2004, "Vortex-Wake-Blade Interaction in a Shrouded Axial Turbine," ASME Paper No. GT-2004-53915.
[16] Gier, J., Stubert, B., Broulliet, B., and De Vito, L., 2003, "Interaction of Shrouded Leakage Flow and Main Flow in a Three-Stage LP Turbine," ASME Paper No. 2003-GT-38025.
[17] Denton, J. D., 1993, "Loss Mechanisms in Turbomachines," ASME J. Turbomach., **115**, pp. 621–658.
[18] Behr, T., Porreca, L., Kalfas, A. I., and Abhari, R. S., 2004, "Multistage Aspects and Unsteady Effects of Stator and Rotor Clocking in an Axial Turbine With Low Aspect Ratio Blading," ASME Paper No. GT2004-53612.
[19] Pfau, A., 2004. "Loss Mechanisms in Labyrinth Seals of Shrouded Axial Turbines," ETH Ph.D. dissertation No. 15226.